Superconductor Science and Technology

PAPER

Prediction of strain, inter-layer interaction and critical current in CORC® wires under axial strain by T-A modeling

To cite this article: K Wang *et al* 2022 *Supercond. Sci. Technol.* **35** 105012

IOP Publishing Superconductor Science and Technology
Supercond. Sci. Technol. **35** (2022) 105012 (16pp) https://doi.org/10.1088/1361-6668/ac8a23

Prediction of strain, inter-layer interaction and critical current in CORC® wires under axial strain by T-A modeling

K Wang[1,2,3], Y W Gao[1,2,*], V A Anvar[3,4], K Radcliff[5], J D Weiss[5,6], D C van der Laan[5,6], Y H Zhou[1,2] and A Nijhuis[3,*]

[1] Lanzhou University, Department of Mechanics and Engineering Science, College of Civil Engineering and Mechanics, Lanzhou, Gansu 730000, People's Republic of China
[2] Key Laboratory of Mechanics on Environment and Disaster in Western China, The Ministry of Education of China, Lanzhou, Gansu 730000, People's Republic of China
[3] Faculty of Science & Technology, University of Twente, 7522 NB Enschede, The Netherlands
[4] University of Wollongong, Institute for Superconducting and Electronic Materials, Wollongong, Australia
[5] Advanced Conductor Technologies LLC, Boulder, CO, United States of America
[6] University of Colorado, Boulder, CO, United States of America

E-mail: ywgao@lzu.edu.cn and a.nijhuis@utwente.nl

Received 22 March 2022, revised 29 June 2022
Accepted for publication 16 August 2022
Published 9 September 2022

Abstract

Superconducting conductors on round core (CORC®) cables and wires can meet the needs of large high-field magnets, such as particle accelerators and compact nuclear fusion machines, due to their simple cabling process, high current-carrying capacity and reliable operation under high mechanical stresses. Many high-field magnets require CORC® cables to carry a current of thousands of amperes in a background magnetic field exceeding 20 T. As a result, the large electromagnetic forces will deform the cable in the axial direction due to hoop stress and in the transverse direction by compressive stress. Therefore, it is essential to determine the irreversible deformation limit of the CORC® cable under axial tensile load and optimize the cabling parameters to potentially extend this limit. Analytical and numerical methods are developed to assess the performance degradation of CORC® wires under axial tensile load. The strain level, interlayer contact pressure and friction and their impact on the critical current are calculated by combining the mechanical response and the T-A method. Analyzing the results shows that the winding angle of the tape and the Poisson's ratio of the inner core are key factors affecting the irreversible tensile strain limit of CORC® wires. The smaller the winding angle and the higher the Poisson's ratio of the inner core, the higher the irreversible tensile strain limit. For multi-layer CORC® wires, the initial contact pressure caused by the cabling process must also be considered. The inter-layer interaction is coupled with the tape strain of each layer. The results of this research can serve as a basis for optimizing and designing CORC® wires with extended irreversible strain limits.

Keywords: HTS cable, CORC®, axial tensile load, inter-layer interaction, critical current reduction, T-A method

(Some figures may appear in colour only in the online journal)

* Authors to whom any correspondence should be addressed.

1. Introduction

The recent development of second-generation high-temperature superconductor (HTS) cables for large-scale applications has made considerable technological advances. They allow operation at magnetic fields exceeding 20 T and at temperatures significantly above the boiling temperature of liquid helium, which is beyond the capabilities of cables made from NbTi and Nb_3Sn [1–3]. Existing large magnets made from superconducting cables include magnetic resonance imaging [4], particle accelerators [5], and nuclear fusion reactors [6]. Many applications required operation at currents of over 5 kA in a background magnetic field of over 20 T [7, 8]. High electromagnetic stress can cause mechanical stability problems and electrical performance degradation. The superconducting layer in REBCO tapes is brittle and deformation beyond the intrinsic axial tensile strain limit ($\varepsilon_{\mathrm{irr}} = 0.45\%$) results in irreversible electrical performance degradation [9, 10]. This limit is far less than the deformation limit of NbTi wires (3%) [3] and close to that of Nb_3Sn wires (0.3%–0.6%) [11].

The existing cables made of REBCO tape include the following four structures: Roebel assembled coated conductor cables [12, 13], twisted-stack slotted core cables [14, 15], twisted stacked-tape cables [16–19] and conductor on round core (CORC®) cables and wires [20]. The CORC® cable contains HTS tapes wound around a core, has a simple production process, strong current carrying capacity, and low AC loss. The strain state of the REBCO layer is determined by the tape strain during the cabling process, the thermal strain of the tape during the cooling process, and the strain introduced by the electromagnetic stress during operation.

To determine the effect of the REBCO tape strain on the CORC® wire performance, Anvar *et al* studied the bending flexibility of CORC® wires by combining experiments with a finite element model and considering the effect of the winding process on the REBCO layer strain [21]. Wang *et al* calculated the nonlinear contact characteristics and deformation of the HTS tape under different winding parameters during CORC® cabling by simulation and theoretical method [22]. van der Laan *et al* conducted uniaxial tensile tests of multilayer CORC® wires in liquid nitrogen, studying the performance degradation of CORC® wires under monotonic and cyclic axial loads [23]. Their latest axial tensile experimental study shows that the CORC® wire can maintain more than 97% of the transport performance at an applied axial tensile strain is as high as 7% through structural optimization [24]. The result was confirmed by initial finite element modeling [25]. Except the mechanical properties, there are also the following studies on the electromagnetic properties of CORC® wires. Wang *et al* calculated the electrical characteristics of CORC® cables by the T-A method, which is based on the magnetic vector potential A and the current vector potential B and often used to describe thin superconducting tapes [26], and their results showed that the AC losses of CORC® layers were affected by the different winding geometry parameters. Yang *et al* analyzed the AC loss of CORC® cables by H-method [27]. Their study found that the losses of CORC® cables are mainly in the core. Lai *et al* proposed J-method and studied the current distribution and AC loss on the surface of HTS tape in CORC® cables under transverse magnetic field [28]. In addition, the latest study by Phifer *et al* also shows that the contact between tapes in CORC® wires greatly influences its electrical properties [29].

Most of the previous work focused on experimental and electromagnetic performance prediction. This paper describes the establishment of a highly detailed three-dimensional model of CORC® wires under applied axial tensile strain by combining theory with the finite element method (FEM) that goes beyond that of [25]. Here, we study the influence of cable winding parameters and inter-layer interaction, such as inter-layer contact pressure and friction of CORC® wires during application of tensile strain. Firstly, the approximate analytical expression of the strain in helical HTS tape, of a single-layer CORC® wire under tensile strain, is given. The strain level of the REBCO layer is calculated for different winding angles and core diameters. The distribution of normal contact force and friction between layers is studied by parameter variation. Secondly, the strain distribution of the REBCO layer between the inner and outer layers at different winding angles is analyzed for a 2-layer CORC® wire. The reduction of the transport performance of the inner and outer layers, caused by tensile strain is calculated with the T-A method. Finally, the initial contact and inter-layer interaction during cabling and applied axial tensile load are considered in detail. The strain level, contact force distribution, and critical current reduction of each layer in optimized CORC® wires with 12 and 14 layers are calculated. Section 2 of this paper outlines the theory and the finite element model. Section 3 provides a discussion of the model results and final conclusions. Table 1 lists the important parameters in the model.

2. Model introduction

2.1. Theoretical model of CORC® wires under axial tensile strain

The tapes wound in a helical fashion around the inner core of the CORC® wire are of the type SCS2030 (width: 2 mm, thickness: 45 μm) produced by Superpower Inc. The change in tape geometry when axial strain is applied to the wire is shown in figure 1(a). Since the tape thickness is far less than its width, the deformation of the tape along its thickness is minor. So, only the tape axial strain along the helical axis is considered here and the gap between tapes is ignored. According to the deformation geometry, and since the tape is thin, the tape strain is approximately the REBCO layer strain, which is:

$$\varepsilon_{\mathrm{Tape}} = \frac{\Delta S}{S} = \frac{\frac{l+\Delta l}{\sin\alpha'} - \frac{l}{\sin\alpha}}{\frac{l}{\sin\alpha}} \approx \frac{\Delta l}{l}\sin^2\alpha + \frac{\Delta r}{r}\cos^2\alpha + \frac{\Delta\varphi}{l} * r\sin\alpha\cos\alpha, \tag{1}$$

Here, $\varepsilon_{\mathrm{CORC}} = \frac{\Delta l}{l}$ is the strain along the tensile direction of the overall cable, $\varepsilon_r = \frac{\Delta r}{r}$ is the strain associated with the

Table 1. Important parameters in the model.

Parameter	Description	Unit	Parameter	Description	Unit
l	CORC® wire length	mm	S	Helical tape length	mm
r	Radius of the core	mm	μ	Friction coefficient	—
α	Winding helix angle	°	ν	Core Poisson's ratio	—
φ	Tape self-rotation angle	°	E	Young's modulus	MPa
t	Thickness of the tape	mm	λ	Lamé constant	MPa
ρ	Radius of helical curvature	mm	f	Friction stress	MPa
F	Winding pre-tension force	N	D	Tape bending stiffness	MPa
p	Contact pressure	MPa	p_i	Contact pressure of layer i on layer $i-1$	MPa
σ_r	Radial stress	MPa	σ_{rk}	Radial stress onto layer k due to tension	MPa
$\sigma_{r(i\to k)}$	Radial stress of layer i on layer k	MPa	p_m	Initial contact pressure on layer m due to cabling	MPa

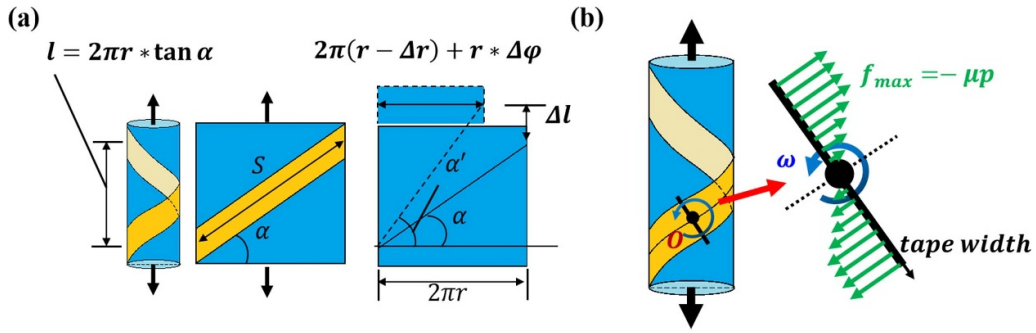

Figure 1. (a) Overview of the change in tape geometry in a CORC® wire under tensile strain. (b) Friction distribution of the helical tape rotating on the core surface.

radial contraction of the cable, $\varepsilon_\varphi = \frac{\Delta\varphi}{l}$ is the rotation angle of the tape cross-section along its axis in unit length. For the helical tape, the rotation angle is usually ignored. When tensile strain is applied to the CORC® wire containing a single tape, the core will contract in the radial direction due to the Poisson's ratio, which is generally smaller than the radial contraction of the helical tape. The thickness of the tape is much smaller than the core radius, so the radial strain can be written as follows:

$$\frac{\Delta r}{r} \approx -\nu\frac{\Delta l}{l},\ (\nu \leqslant \tan^2\alpha). \tag{2}$$

Here, the Poisson's ratio of the core must be less than $\tan^2\alpha$, which is the equivalent Poisson's ratio of a helical tape. When the Poisson's ratio of the core is greater than $\tan^2\alpha$, the radial contraction of the core is higher than that of the tape, and the tape does not maintain contact to the core. The tape strain is calculated by combining (2) and (1) and ignoring the tape rotation:

$$\varepsilon_{\text{Tape}} \approx \varepsilon_{\text{CORC}}(\sin^2\alpha - \nu\cos^2\alpha),\ (\nu \leqslant \tan^2\alpha). \tag{3}$$

Then the contact pressure between the tape and the core, originating from the CORC® wire strain, is:

$$p = \frac{E\varepsilon_{\text{Tape}}t\cos^2\alpha}{r}. \tag{4}$$

In addition, the tape rotates on the core surface (see figure 1(b)). The displacement is almost zero in the tape center and the maximum is at the tape edge. The maximum friction stress is:

$$f = -\mu p. \tag{5}$$

Equations (2)–(5) ignore that the multi-layer interaction is only valid in the case of a single-layer CORC® wires. When tension is applied to multi-layer CORC® wires (see figure 2), the problem is more complex, as radial contraction and contact forces between layers vary. The following equation can estimate the influences from inter-layer interactions on radial contractions between each layer [30]:

$$\frac{\Delta r}{r} = -\frac{\nu_k}{\lambda_k}\left(\sigma_{rk} + \lambda_k\frac{\Delta l}{l}\right). \tag{6}$$

Here $\lambda_k = \frac{E\nu_k}{(1+\nu_k)(1-2\nu_k)}$ is the Lamé constant of tape layer k, r is the core radius, r_k is the radius of layer k, and σ_{rk} is the radial stress on layer k due to tension. In a multi-layer CORC® wire under tension, each layer will add to the force applied to the inner layer.

When p_i is the contact force of layer i onto layer $i-1$, the stress applied by layer i onto layer k is:

$$\sigma_{r(i\to k)} = -p_i\frac{1-(r_k/r_0)^{-2}}{1-(r_i/r_0)^{-2}} \tag{7}$$

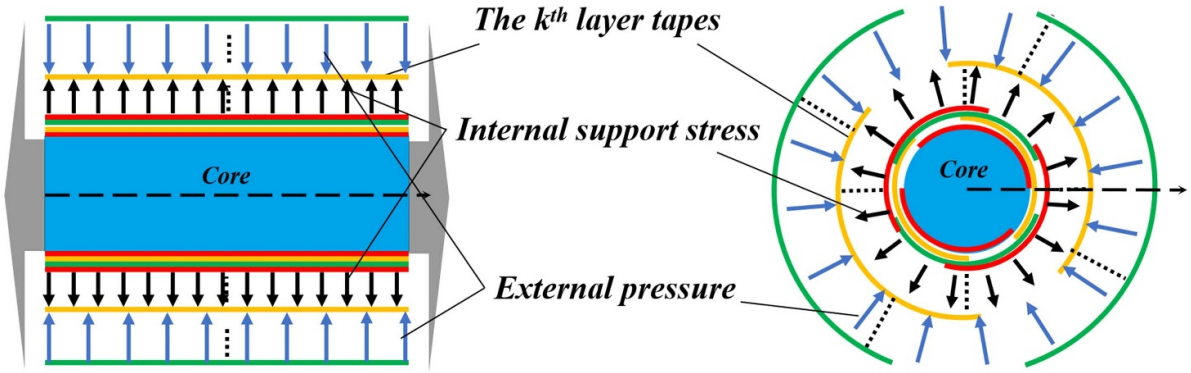

Figure 2. Diagram of inter-layer interaction during stretching of multi-layer CORC® cable.

$$\sigma_{rk} = \underbrace{-\sigma_{r(k\to k-1)} - \sigma_{r(k+1\to k-1)} - \ldots - \sigma_{r(12\to k-1)}}_{\text{The support force of the inner layer on layer k}} + \underbrace{\sigma_{r(k+1\to k)} + \sigma_{r(k+2\to k)} + \ldots + \sigma_{r(12\to k)}}_{\text{The pressure of the outer layer onto layer k}}. \quad (8)$$

It can be seen that for only one layer of tape, $r_k = r_i \approx r$, the contact pressure p is relatively small compared to $\lambda\frac{\Delta l}{l}$, and equation (6) can be simplified to equation (2).

Therefore, the inter-layer interaction of multi-layer CORC® wires under axial tensile strain can be calculated by formulas (4)–(8). The actual strain of each layer is calculated by formulas (6) and (1). The layer contact is coupled to the layer strain and the problem can only be solved numerically.

2.2. Initial contact pressure caused by the cabling process

In the process of CORC® cabling, several HTS tapes are helically wound onto the central core under a defined winding tension. Having the asymmetrically positioned REBCO layer on the inside, facing the core, an additional compressive strain is introduced into the REBCO layer, improving the axial tensile critical strain of the CORC® wire to a certain extent. This work focuses on the effect of CORC® wires under axial tensile load, while the pre-strain caused by the cabling process is neglected. However, the pressure exerted by the outer tapes onto the inner layers during the CORC® cabling process is considered. For a single-layer CORC® wire, the contact pressure resulting from the cabling process is around 1 MPa, which has little influence on the cable tensile results. However, for multi-layer CORC® wires, the pressure will be superimposed and this significantly affects the axial tensile behavior. The nonlinear and non-uniform contact between layers is ignored to simplify the calculation. Then, the contact pressure of each layer after cabling can be calculated by equations (9)–(11) [22], while the calculated result of the contact pressure of each layer based on the cable winding parameters of 12-layer and 14-layer CORC® wires [23] is shown in figure 3:

$$p = \frac{F\left(1 - \frac{D}{2F\rho^2}\right)}{\rho w} \quad (9)$$

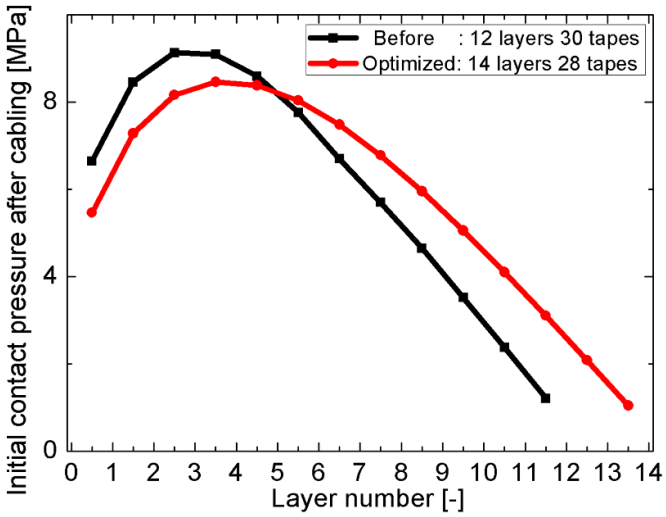

Figure 3. The initial contact pressure of each layer after cabling of 12-layer and 14-layer CORC® wires.

$$\sigma_{r(i\to m)} = p_i \frac{1 - (r_m/r_0)^{-2}}{1 - (r_i/r_0)^{-2}} \quad (10)$$

$$p_m = \sigma_{r(m+1\to m)} + \sigma_{r(m+2\to m)} + \ldots + \sigma_{r(i\to m)} + \ldots + \sigma_{r(12\to m)}. \quad (11)$$

2.3. T-A FE model of CORC® wires under axial tension

A three-dimensional finite element model is established in three main steps, using commercial software COMSOL, as illustrated in figure 4. The first step is to establish the overall structure of the CORC® wire. The HTS tape and core are solid units, calculated within the solid mechanical module. The ends of the tapes and core are bound as coupling points on both ends of the cable. One end is fixed while the other end is moved over a specified displacement. Next, helical shells without thickness represent the REBCO layer in the HTS tape, which is cut from the middle part of the solid model geometry can eliminate stress concentrations caused by boundary conditions during strain application. Then, the

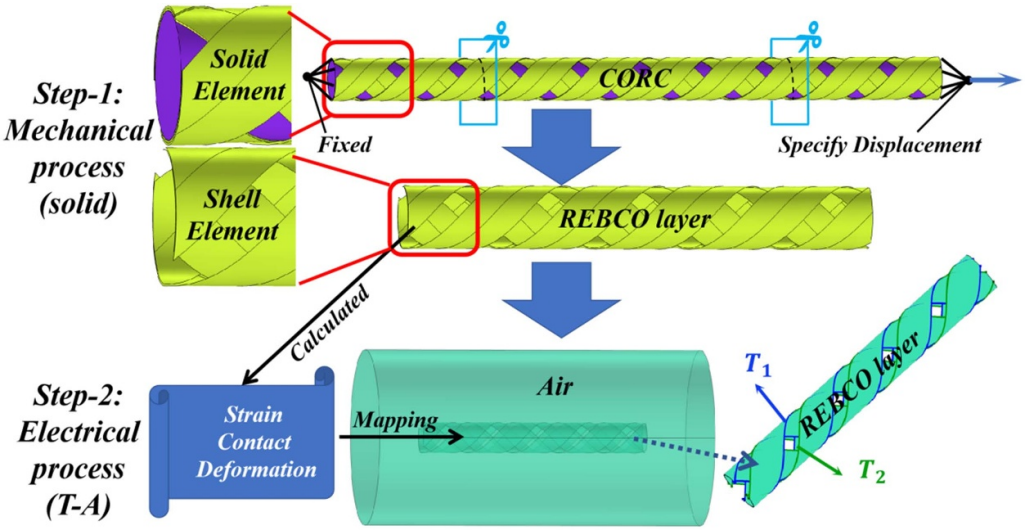

Figure 4. Three-dimensional finite element (FE) model of the T-A method considering a cable tensile loading process.

strain and deformation states calculated in step-1 are implemented to the shell. Subsequently, the deformed helical shell in step-2 is wrapped with a cylindrical air domain. Finally, the T-A method-based model can calculate the critical current degeneration of the tape in CORC® wires under tension.

Here, we briefly review the specific equations of the T-A method, defining the current vector:

$$\mathbf{J} = \nabla \times \mathbf{T}, \tag{12}$$

$$\boldsymbol{T}_1 - \boldsymbol{T}_2 = \frac{\boldsymbol{I}_{\mathbf{apply}}}{\boldsymbol{t}_{\mathbf{REBCO}}},$$

where I_{apply} is the applied direct current:

$$I_{\mathrm{apply}} = I_0 \mathrm{rn}\,(\mathrm{time})\,. \tag{13}$$

Here, $\mathrm{rn}\,(\mathrm{time})$ is a function that increases the transport current linearly with time. The magnetic field is:

$$\mathbf{B} = \nabla \times \mathbf{A}. \tag{14}$$

The Faraday's law of the electromagnetic induction is:

$$\nabla \times \boldsymbol{E}\,(\mathbf{J}) = -\frac{\partial \boldsymbol{B}}{\partial \boldsymbol{t}}. \tag{15}$$

The Ampere's law for the magnetic potential loss representation is

$$\nabla \times \nabla \times \mathbf{A} = \mu \mathbf{J}. \tag{16}$$

The electric field as a function of current density is

$$E\,(\mathrm{J}) = E_0 \left(\frac{|\mathrm{J}|}{J_c\,(\varepsilon)} \right)^n \frac{\mathrm{J}}{J_c\,(\varepsilon)}, \tag{17}$$

$$J_c\,(\varepsilon) = J_{c0} * T(\varepsilon)\,. \tag{18}$$

Here, $T(\varepsilon)$ is the fitting function of a straight tape under self-field conditions [9], represents the impact of the strain field, which is:

$$T(\varepsilon) = \begin{cases} 1 - 6918|\varepsilon|^{2.2\pm0.2}\,, & \varepsilon \leqslant 0.6\% \\ -202.52\varepsilon + 2.1262\,, & \varepsilon > 0.6\% \end{cases}. \tag{19}$$

In this way, the critical current reduction of all layers of the CORC® wire can be calculated after tensile strain is applied, and the local deformation from the inter-layer contact can also be considered for the multi-layer tape.

2.4. Model parameters and experimental validation

Specific material parameters were fitted using the experimental curve shown in figure 5(a). It shows the tensile stress versus strain curve of two types of core materials in liquid nitrogen and the results of the corresponding FEM simulation [24]. The linear reinforced plasticity model is used for the cores. Figure 5(b) shows the critical current reduction comparison between experiment and FE model for a single straight tape [9]. The irreversible tensile limit of the tape is 0.45%, and 0.6% in the figure is considering the cooling thermal strain (−0.15%). The tape is considered an isotropic homogeneous material, and the ideal plasticity model is used. All the parameters in the FE model are listed in table 2.

The winding structure of the 12-layer CORC® wire from the experiment described in [23] was modeled. Figure 6 shows the points representing the experimental results and the solid lines are the model calculations. It can be seen that the initial contact and friction between layers must be considered when the multi-layer CORC® cable is strained. The initial contact pressure between tapes will increase the Young's modulus and the yield limit of the cable. The results also confirm the FE model.

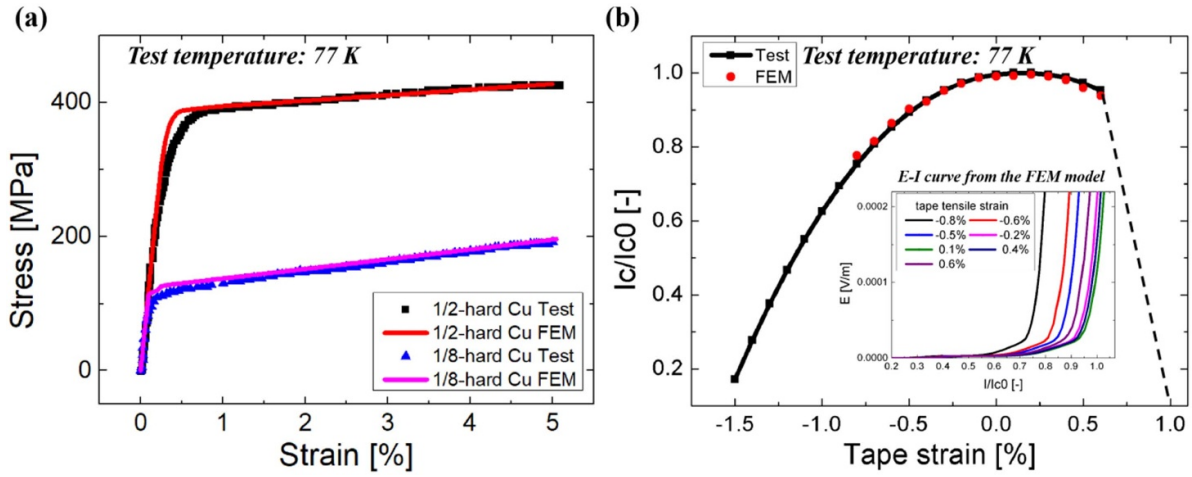

Figure 5. (a) Experimental tensile stress–strain curves and FEM simulation of two different cores under 77 K. (b) Experimental and FEM results of critical current reduction of a straight tape as a function of axial tensile strain.

Table 2. Material parameters in the model.

Parameter	Value
Young's modulus of SCS2030 tape (77 K)	180 GPa
Young's modulus of 1/8 hard Cu core (77 K)	130 GPa
Young's modulus of 1/2 hard Cu core (77 K)	130 GPa
Plastic yield stress of SCS2030 tape (77 K)	1091 MPa
Plastic yield stress of 1/8 hard Cu core (77 K)	110 MPa
Plastic yield stress of 1/2 hard Cu core (77 K)	390 MPa
Poisson's ratio of the tape	0.3
Poisson's ratio of the core	0.3

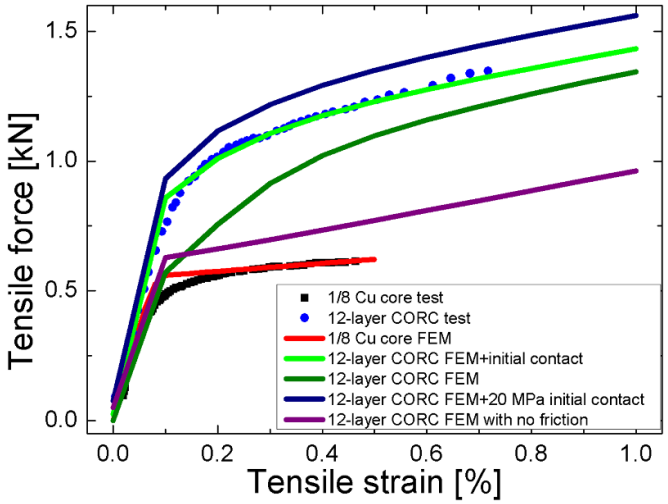

Figure 6. Comparison of experimental and FEM force versus strain curves for a 12-layer CORC® wire.

3. Results and discussion

3.1. Result of single-layer CORC® wires under applied tensile strain

The mechanical behavior of a single-layer CORC® wire under applied tensile strain is calculated along the tape length. The locations for which strain, contact force, and friction are calculated are indicated by the lines shown in figure 7.

As shown in figure 8, the results of the FEM model show stress concentrations at the ends of the cable, while the strain and normal contact force are uniform in the middle of the cable. Therefore, the tape strain of the middle part of the cable can be used as a criterion of tape deformation due to CORC® wire tensile strain. In addition, figures 8(c) and (d) show that the frictional force at the center of the tape along the width direction is almost zero when axial tensile strain is applied to the single-layer CORC® wire. The maximum frictional force occurs at the edges of the tape and the helical tape will rotate around the tape axis on the core surface. Moreover, the upper limit of friction is the sliding friction set by the model, and its value is μp. Also, for single-layer CORC® wires, the initial contact pressure has little influence on the results. Therefore, only the impact from the cooling and tensile strain process is considered, and the initial strain state of the tape in the cabling process is ignored in all following calculations.

3.1.1. Tape tensile strain as a function of CORC® wire tensile strain. The effect of CORC® wire tensile strain on the deformation and contact pressure of the tape in the cable are calculated using the FEM model. A single layer CORC® wire with 45° winding angle and uniform strain of −0.15% due to cool down is considered. It can be seen from figure 9 that when the cable strain increases, the tape strain and the contact force between the tape and the core both increase. For a single layer CORC® wire, the initial contact force has little effect and can be ignored in subsequent parameterization calculations. Equations (3) and (4) can be used to calculate the tape strain and the contact pressure. The plasticity of the core causes a deviation at high strain. The stronger the core (the higher the yield limit), the higher the tape strain and the normal contact pressure under the same CORC® wire tensile strain.

3.1.2. Effect of the diameter and Poisson's ratio of the core. Figure 10 shows the tape strain for different core diameters in a single-layer CORC® wire in which the tapes are wound

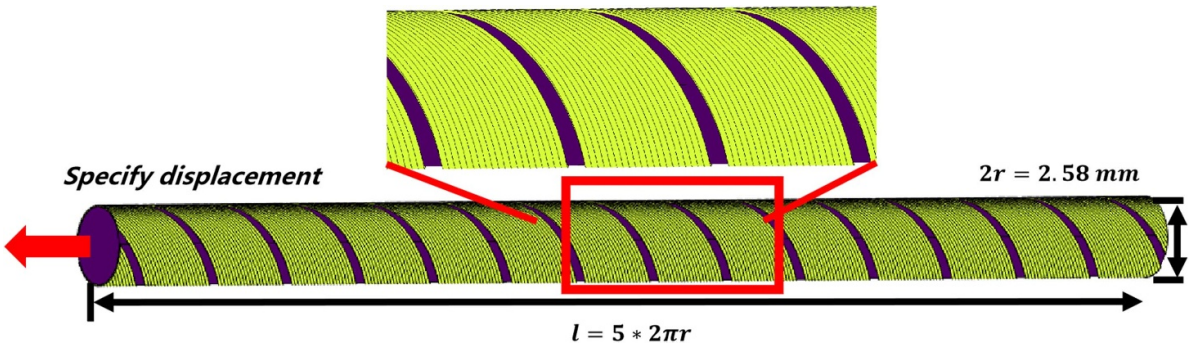

Figure 7. FE model of single layer CORC® wire.

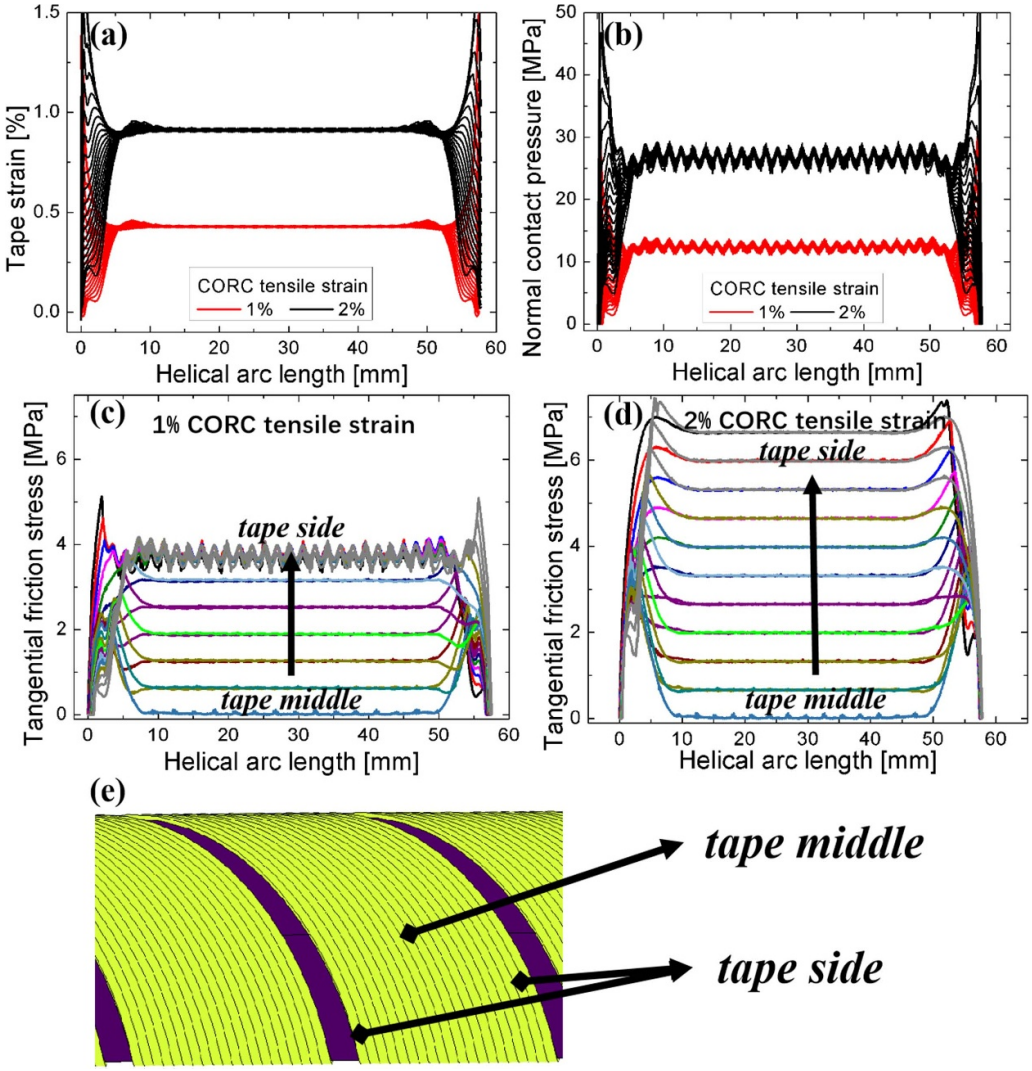

Figure 8. Mechanical behavior of the tapes in a single-layer CORC® wire after 1% and 2% tensile strain has been applied to the wire. (a) Tape strain along the helical arc direction. (b) The contact pressure between the tape and the core. (c) Friction stress between the tape and the core under 1% cable tensile strain. (d) Friction stress between the tape and the core under 2% cable tensile strain. The initial contact pressure and tape strain from cabling are ignored, while the following parameters were used in the model: $\alpha = 45°$, r = 1.29 mm, $l = 5 \times 2\pi r$, $\mu = 0.3$, $\nu_{\text{core}} = 0.3$, $\nu_{\text{tape}} = 0.3$.

at an angle of 40°. It can be seen that the tape strain does not change significantly with the core diameter variation. It is shown in figure 10(b) that the Poisson's ratio of the core has an impact on the tape strain. When the Poisson's ratio of the core increases, the tape strain decreases, which follows directly from equation (3).

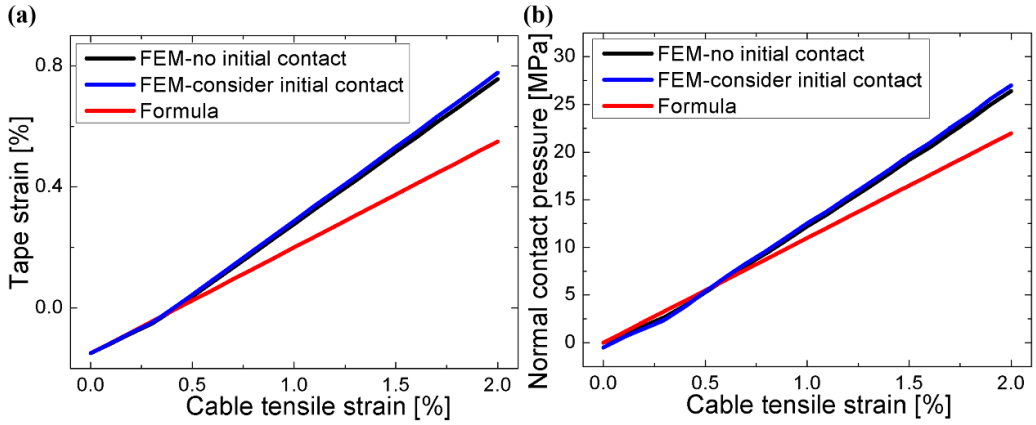

Figure 9. (a) Calculated tape strain along the helical arc direction. (b) Contact pressure between the tape and the core as a function of strain applied to a single-layer CORC® wire. The initial contact pressure and tape strain from cabling are ignored, while the following parameters were used in the model: $\alpha = 45°$, r = 1.29 mm, $l = 5 \times 2\pi r$, $\mu = 0.3$, $\nu_{\text{core}} = 0.3$, $\nu_{\text{tape}} = 0.3$.

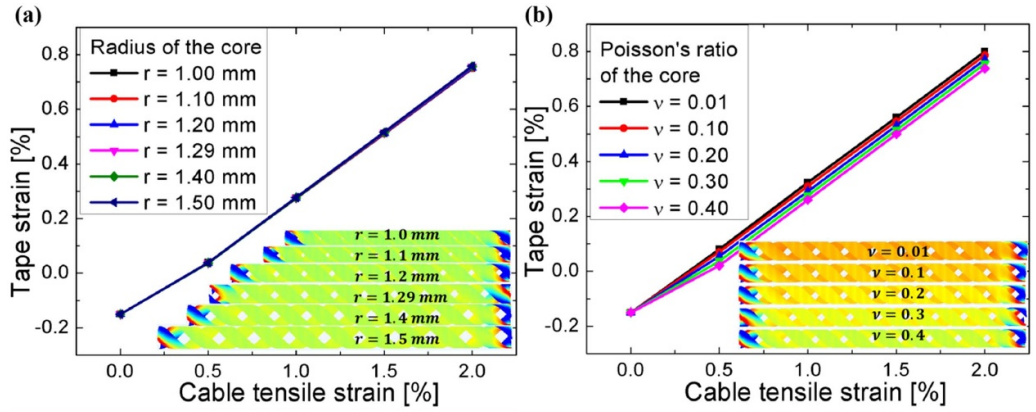

Figure 10. Tape strain versus cable axial tensile strain of a single layer CORC® wire (a) for different core diameters, and (b) for different Poisson's ratios of the core. The initial contact pressure and tape strain from cabling are ignored, while the following parameters were used in the model: $\alpha = 40°$, $l = 5 \times 2\pi$r, $\nu_{\text{tape}} = 0.3$.

3.1.3. Effect of tape winding angles. The winding angle of tapes in a CORC® wire under tensile axial load has a significant effect on the tape strain. This is shown in figure 11(a), where it is shown that the tape strain increases with winding angle. It should be noted that the winding angle affects the winding pitch and the number of tapes that can be wound in single layer, but these have little effect on the tensile behavior of the cable. Therefore, the results in figure 11 are all calculated at four pitch lengths and two tapes wound in one layer. The tape axial stress as a function of cable tensile strain is given in figure 11(b). The lower winding angle results in the tape to remain in the elastic regime under high CORC® tensile strain. It can thus be concluded that the lower the winding angles result in a better tensile property of the CORC® wire. Also, a maximum contact pressure between tape and core occurs at 50° winding angle (see figure 11(c)). The analytical formulas (3) and (4) can estimate the tape strain and tape-core contact pressure with reasonable accuracy in the low CORC® tensile strain range. At higher applied CORC® tensile axial strain levels, a significant error can occur, mainly due to the plasticity of the core.

Considering the cooling process that induces an additional tape strain of −0.15%, formula 3 can be used to estimate the tensile strain limit of a single-layer CORC® wire for different tape winding angles and different Poisson's ratios of the core. Figure 12(a) shows that the cable's irreversible tensile strain limit will decrease when the winding angle increases. The REBCO layer will be damaged when exceeding the irreversible strain limit and permanent critical current degradation will occur. This shows that for a CORC® wire in which the tapes are wound at angles of 30°–35°, the critical tensile strain limit increases from 2% to 10%, compared to a cable in which the tapes are wound at 40°–45°. In addition, an increase in the Poisson's ratio of the core can also significantly increase the tensile strain limit of CORC® wire. The radial contraction of the core must be less than that of the helical tape, for which $\nu \leqslant \tan^2\alpha$. It should be noted that the materials with high Poisson's ratios are mostly soft materials or flexible structures.

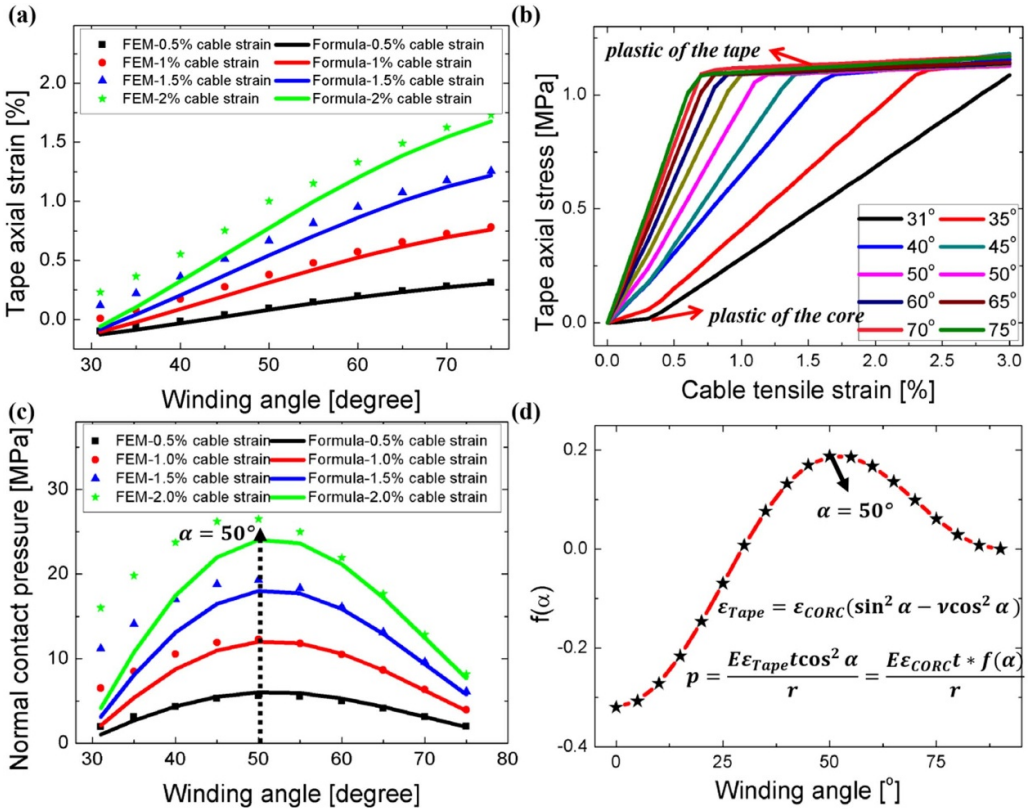

Figure 11. (a) Tape strain as a function of winding angle at different strains applied to a single-layer CORC® wire. (b) Stress–strain relationship of the tapes wound at different winding angles. (c) Contact pressure between the tape and the core as a function of winding angle. (d) Theoretically, it can be proven that the normal contact pressure is the maximum at 50°. The initial contact pressure and tape strain from cabling are ignored, while the following parameters were used in the model: r = 1.29 mm, $l = 5 \times 2\pi r$, $\mu = 0.3$, $\nu_{\text{core}} = 0.3$, $\nu_{\text{tape}} = 0.3$.

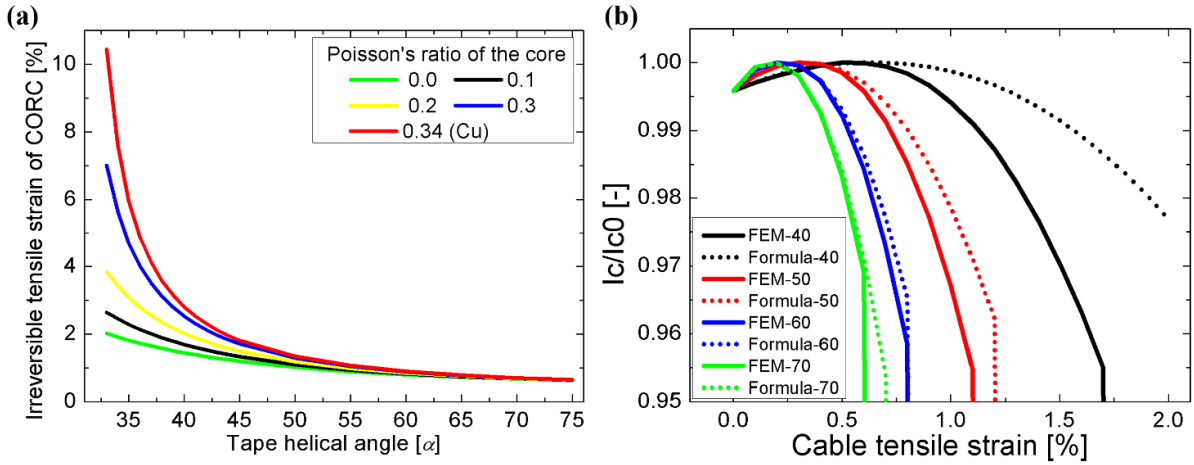

Figure 12. (a) Analytical prediction of the irreversible CORC® tensile strain limit with different core material Poisson's ratios, versus the tape helix winding angle. (b) FEM results and analytical prediction of the critical current reduction of a single-layer CORC® wire at different helical angles, versus applied tensile strain.

Although the irreversible tensile strain limit of CORC® wires can be increased with such materials, their overall strength will be lower.

Finally, the critical current reduction of a single-layer CORC® wire under tension is calculated for different winding angles and the results are shown in figure 12(b). The solid lines represent the results of the numerical model, and the dashed lines are produced from the analytical formulas. The analytical formulas can predict the critical current reduction quite well for low applied tensile strains and high winding angles.

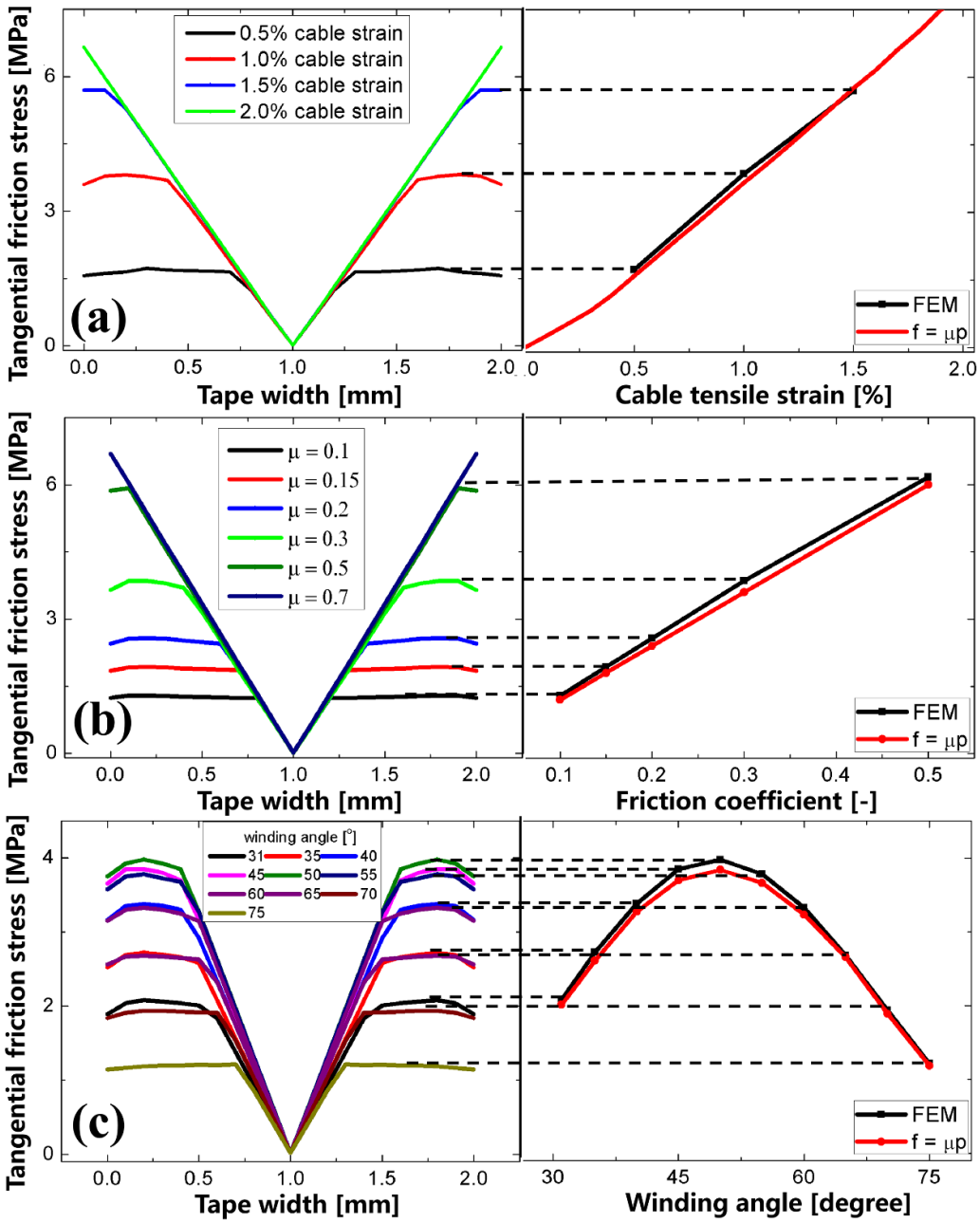

Figure 13. The distribution of the friction along the tape width (a) for different tensile strains applied to the CORC® wire, (b) for different coefficients of friction, and (c) for different winding angles. The initial contact pressure and tape strain from cabling are ignored, while the following parameters were used in the model: r = 1.29 mm, $l = 5 \times 2\pi r$, $\nu_{\text{core}} = 0.3$, $\nu_{\text{tape}} = 0.3$.

Nevertheless, in the high tensile strain and lower winding angle ranges, the deviation is higher because the core plastic deformation is not accounted for in the analytical formulas.

3.1.4. Tape friction in CORC® wires under axial strain. The friction characteristics between tape and core are discussed for the case of a CORC® wire with two tapes wound into a single-layer under applied axial tensile strain. The influence of the CORC® tensile strain, friction coefficient, and winding angle is investigated. The results are summarized in figure 13. The tangential friction stress increases progressively towards both tape edges with increasing CORC® tensile strain until the maximum friction is reached (see figure 13(a)). When the CORC® tensile strain reaches 2%, the friction stress increases linearly from the tape center line towards the edges, and does not reach a plateau. Figure 13(b) shows the distribution of the friction along the tape width for different friction coefficients. With the increase of friction coefficient, only the maximum (plateau) friction towards both tape edges is increased, and the linear distribution of the stress across the tape width (slope of the curve) remains the same. When the winding angle increases from 30° (see figure 13(c)), the maximum friction stress increases initially and decreases after passing an angle of about 50°. In addition, the curve's slope of the stress

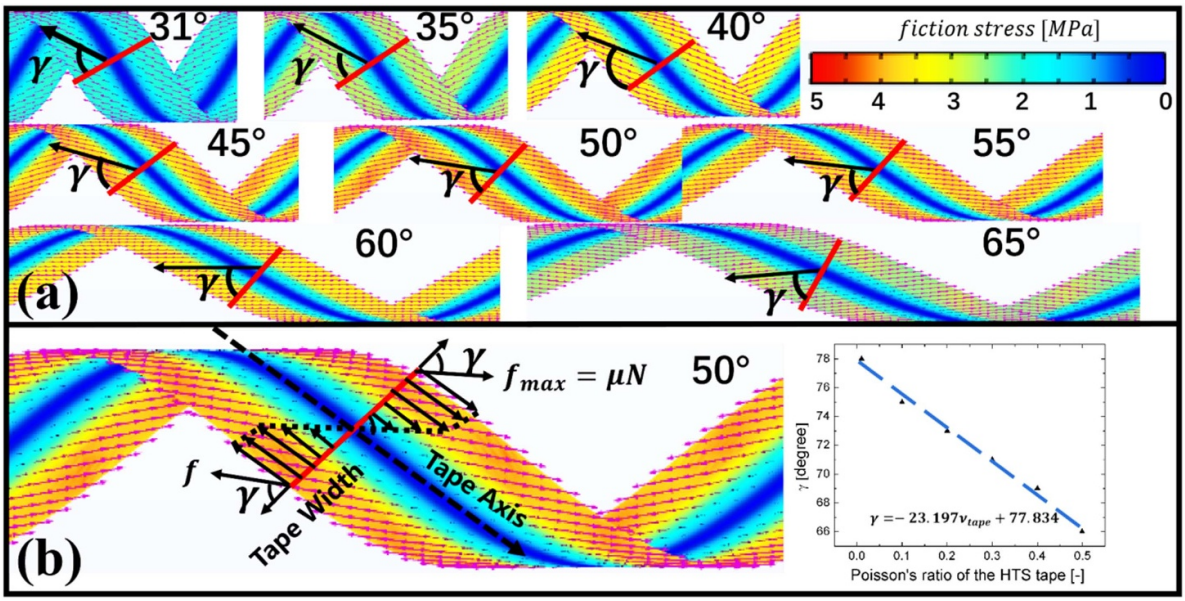

Figure 14. (a) The friction stress distribution for different winding angles. (b) The influence of the tape's Poisson's ratio on the direction of the friction stress.

distribution towards the tape ends changes. It is noteworthy that the direction of the friction stress is not along the helical axis of the tape but occurs at an angle γ with respect to the tape axis (see figure 14(a)). The angle γ remains the same for different winding angles, but changes for different Poisson's ratios of the tape; a linear fit for this relation is shown in figure 14(b). The reason is that when the CORC® cable is axially strained, the tape is also elongated along its axis and at the same time contracts along its width due to the tape Poisson's ratio. In addition, the influences of core radius and tape width were also calculated by this model but are not shown in detail. The core radius almost had no influence on the tape strain but was inversely proportional to the tape-core contact pressure. The core radius increases, the contact pressure and the maximum friction decreases. The tape width would extend the maximum friction range at the tape edge.

3.2. Two-layer CORC® wire under tensile load

For a two-layer CORC® wire, the critical current density (J_c) degradation under applied tensile load is studied. The deformed geometry of a two-layer CORC® wire under axial tension and the strain distribution of the REBCO layer, considering the core and layers interaction, are all mapped to the T-A module. The strain distribution of the two-layer CORC® wire is calculated for applied cable tensile strain levels of 0.5%, 1.0%, 1.5% and 2.5%. The results are shown in figures 15(a) and (b), illustrating the local bending at the gaps between tapes in each layer of 0.54 mm, which is the direct cause for the degradation of the outer tapes. The friction of the two-layer CORC® wire during strain application is shown in figure 15(c). The color distribution in the figure is the normal contact force and the arrow direction is the direction of friction. It can be seen that a friction 'vortex' exists at the contact position between inner and outer layers, which is caused by the mutual dislocation between the adjacent layers when the cable is strained. In addition, the distribution of the strain in the REBCO layer and that of the critical current reduction after tensile loading is shown in figure 16.

The axial tensile load on the cable can have a significant effect on the transport performance of the tapes. The J_c reduction of the inner tapes is more severe than that of the outer tapes. The reason for this is that when the multi-layer CORC® wire is strained, the outer helical tape will contract radially, while the radial contraction of the core is limited, so strain superposition will be accumulating towards the innermost tape, resulting in the largest I_c reduction. The outer tape's largest reduction location is at the location of the gaps between the tapes in each layer due to localized bending. When the cable applied tensile load exceeds 2.5%, the irreversible degradation area near the gap has expanded along the entire tape cross-section.

3.3. Result of multi-layer CORC® wires under applied tensile strain

3.3.1. 12-Layer CORC® wire under tensile load. The 12-layer CORC® wire in the experiment performed by Advanced Conductor Technology LLC [23] is adopted for our multi-layer model. The FEM calculation and the experimental results are shown in figure 17(a), after I_c testing of separate extracted tapes from all layers, revealed that when the cable applied tensile strain reached 1.5%, the critical current degradation in the seventh tape layer was the largest. The critical current degradation shown by the solid line is calculated from the average strain in the FEM model. When the average strain is less than the irreversible strain, the critical current degradation calculated by the FEM model is always less because the tape strain has positive and negative regions. Figure 17(b) shows

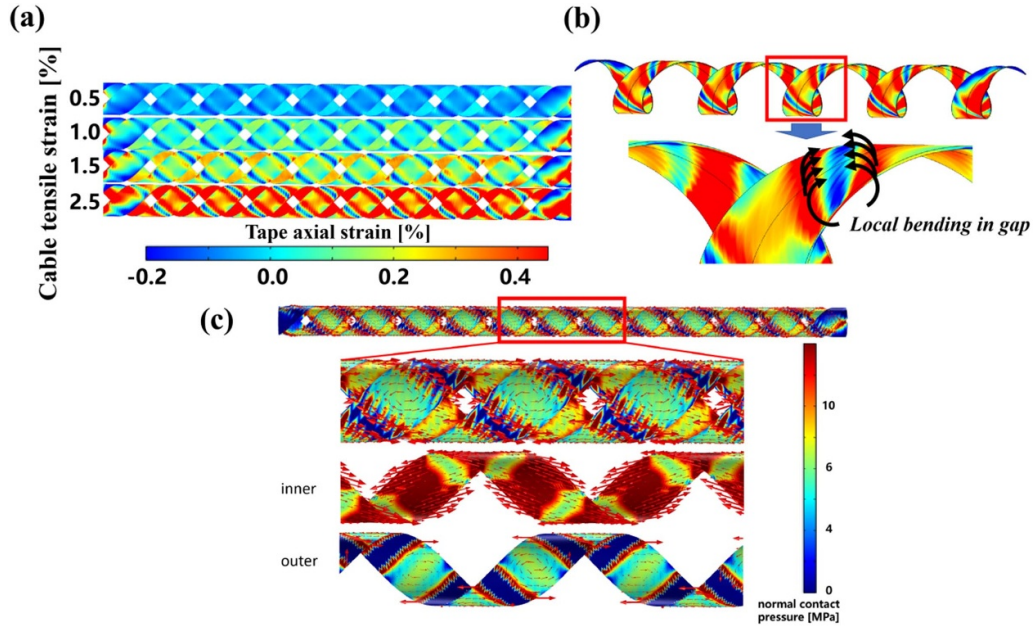

Figure 15. (a) The strain distribution of the two layers of tape (solid element) under 0.5%, 1.0%, 1.5%, and 2.5% applied cable tensile strain. (b) The local bending of the outer tape at the gaps of 0.54 mm. (c) The friction of the two-layer CORC® wire during stretching. The initial contact pressure and tape strain from cabling are ignored, while the following parameters were used in the model: $\alpha = 45^{\circ}$, r = 1.29 mm, $l = 5 \times 2\pi r$, $\mu = 0.3$, $\nu_{\text{core}} = 0.3$, $\nu_{\text{tape}} = 0.3$.

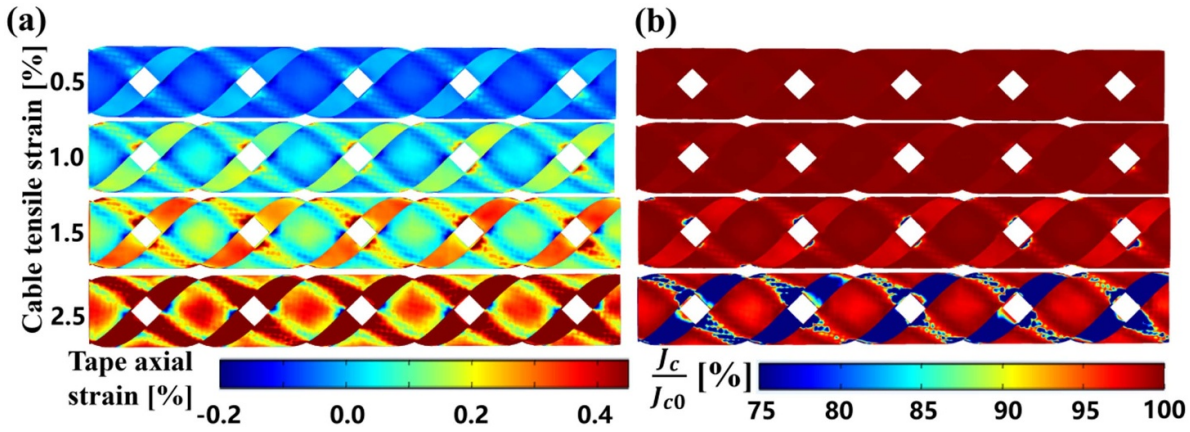

Figure 16. (a) The strain distribution of the two layers of REBCO (shell element) under 0.5%, 1.0%, 1.5%, and 2.5% applied cable tensile strain. (b) The critical current reduction distribution of inner and outer REBCO layers. The initial contact pressure and tape strain from cabling are ignored, while the following parameters were used in the model: $\alpha = 45^{\circ}$, r = 1.29 mm, $l = 5 \times 2\pi r$, $\mu = 0.3$, $\nu_{\text{core}} = 0.3$, $\nu_{\text{tape}} = 0.3$.

the average strain level of each tape layer when the cable is strained. Due to the inter-layer interaction, the tape strain variation trend is different. The average strain level of the seventh layer tape is always the largest.

Figure 18 shows several numerical model calculation results of the average contact stress and tape axial strain in the tape layers, following the 30-tape conductor layout of [23] with tape angles of 30°–47° and for the case in which all layers would be wound at an angle of 45°. The figure also shows the case in which the 3rd and 10th layers are wound at 35°, and all other layers at 45° angle. It also includes the case in which the 9th layer is wound with 35°, and all others with 45°. The average contact stress and tape axial strain distributions, as calculated with the FE model, clearly point out the significance of the choice of the layer winding angle on the strain concentration and the potential to optimize that. In addition, the calculation results of formula 6 are also shown in the figure (see curve with red triangle markers). This result is obtained by substituting the inter-layer contact force as calculated by FEM into formula 6. When the winding angle of the adjacent tape layers changes considerably, the radial shrinkage of the two layers becomes entirely different. As a result, local excessive strain concentrations are created by inter-layer compression. The analysis shows that for multi-layer CORC® wires,

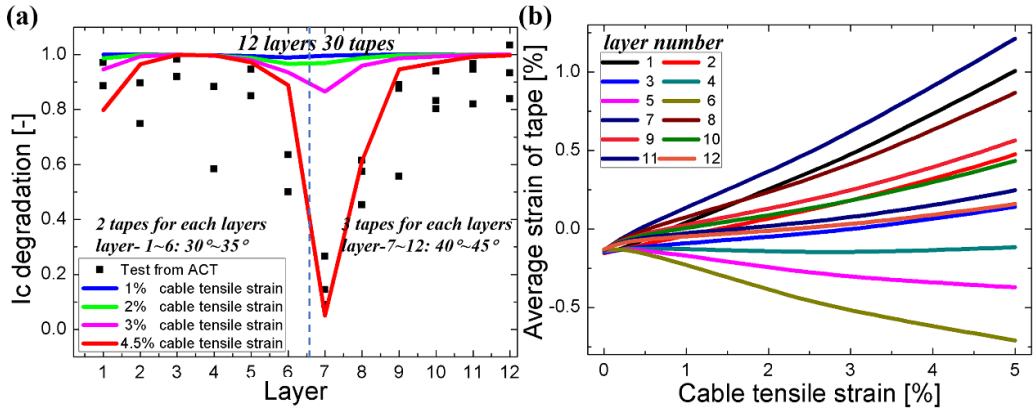

Figure 17. (a) The 12-layer CORC® wire in the experiment performed by Advanced Conductor Technology LLC [23]. The blue dashed line separates the layers that contain two tapes each (left) from those that contain three tapes each (right). (b) The average axial strain of each tape layer as a function of cable tensile strain.

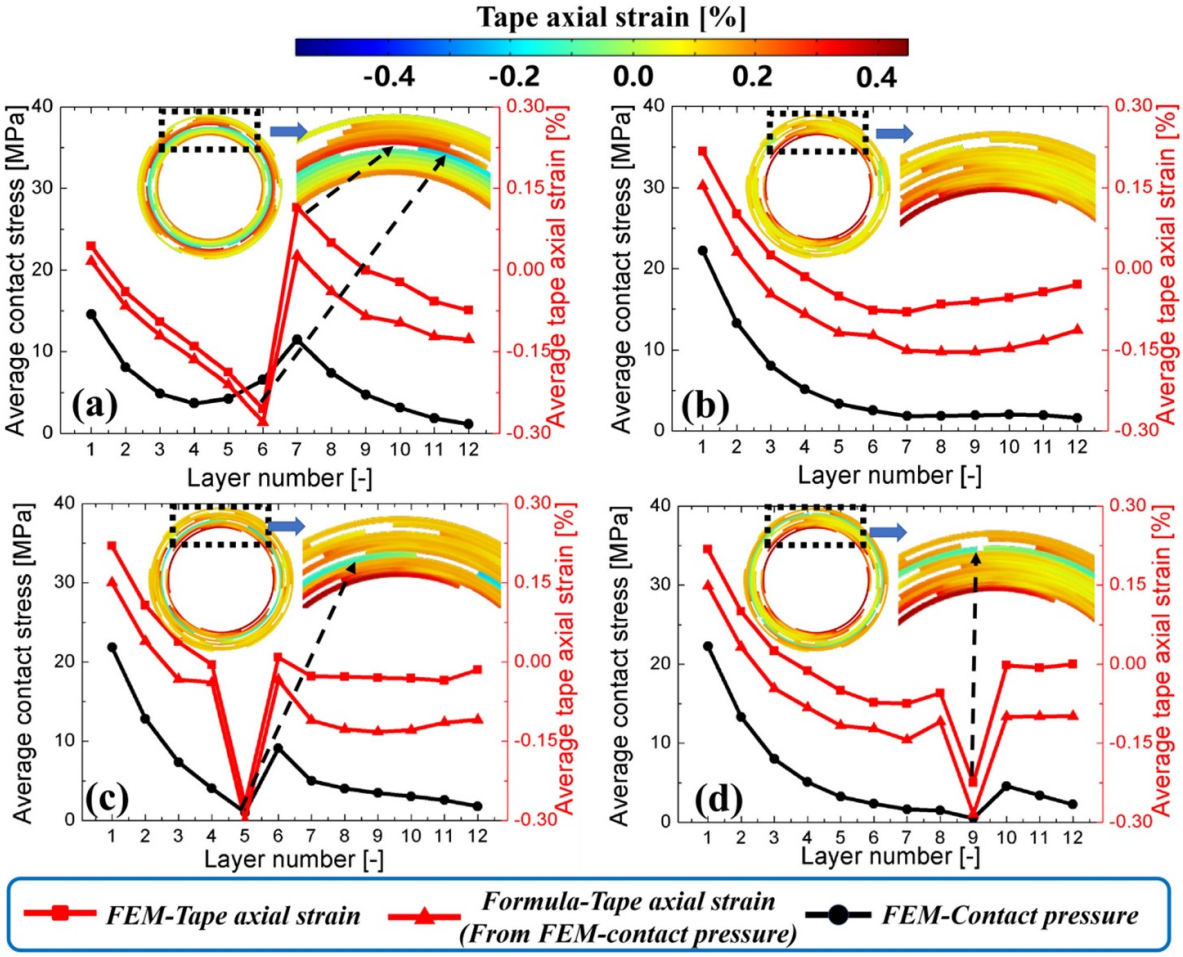

Figure 18. Numerical model calculation results of the average contact stress and tape axial strain, (a) in the tape layers following the 30-tape CORC® wire layout from [23]. (b) In case all layers are wound at an angle of 45°, (c) in case the 3rd and 10th layers are wound at an angle of 35° and all other layers at 45°, and (d) in case the 9th layer is wound at an angle of 35°, and all others with 45°. The initial contact pressure and tape strain from cabling are ignored, while the following parameters were used in the model: $\alpha = 45°$, r = 1.29 mm, $l = 5 \times 2\pi r$, $\mu = 0.3$, $\nu_{\text{core}} = 0.3$, $\nu_{\text{tape}} = 0.3$.

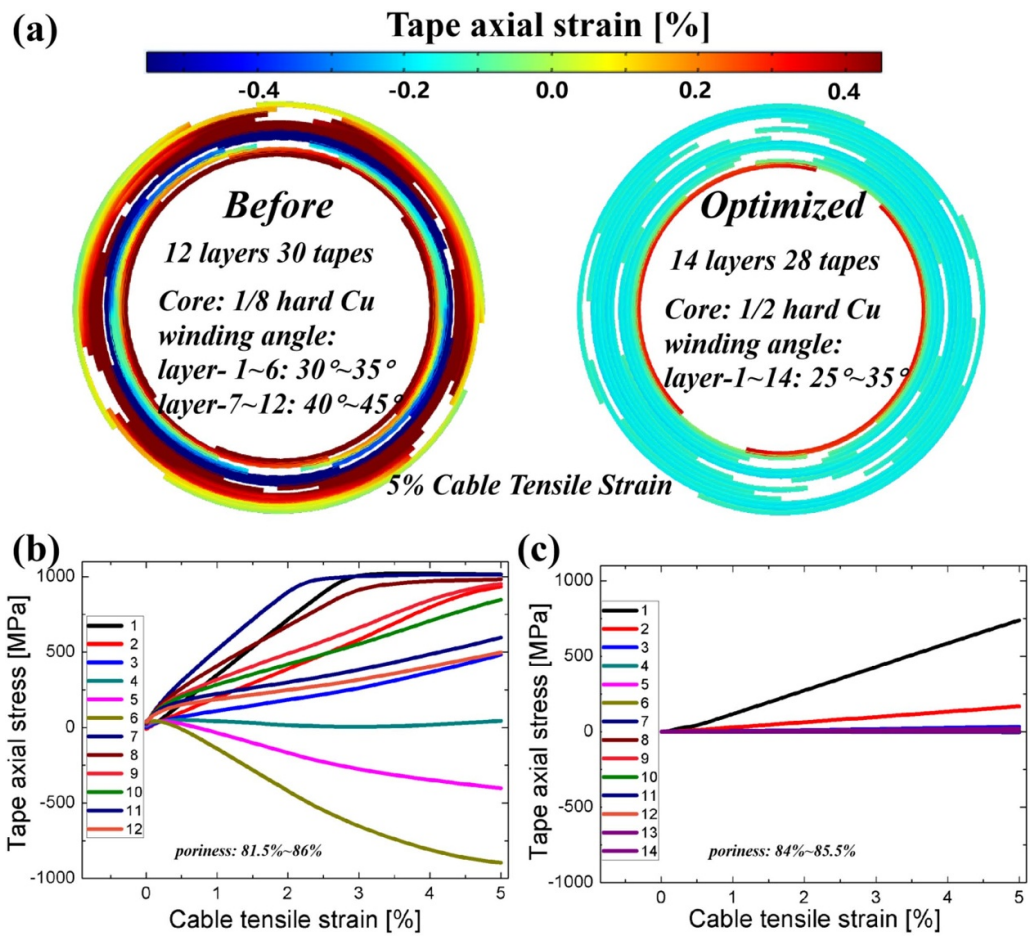

Figure 19. (a) The strain distribution in the cross-section of the 12-layer and optimized 14-layer CORC® wires under 5% applied axial tensile cable strain. (b) The stress–strain curve of each tape layer of the 12-layer and (c) optimized 14-layer CORC® wires. The initial contact pressure from cabling is considered, while the following parameters were used in the model: $\alpha = 45°$, r = 1.29 mm, $l = 5 \times 2\pi r$, $\mu = 0.3$, $\nu_{\text{core}} = 0.3$, $\nu_{\text{tape}} = 0.3$.

the change in winding angles of subsequent layers should be minimized.

3.3.2. Optimized 14-layer CORC® wire under tensile load. The performance of an optimized 14-layer CORC® wire, with winding angles of 25°–35° and only a slight change in the winding angle of adjacent layers, was recently tested under axial tensile strain [23]. The CORC® wire maintained 98% of its critical current at an axial tensile strain of 7%. Figure 19 shows the tape axial stress and the strain distribution across the REBCO layers of the optimized 14-layer CORC® wire under 5% axial strain, compared with the 12-layer CORC® wire from the previous section. The deformation of the superconducting REBCO layers and the tape axial stress in the optimized 14-layer CORC® wire is considerably smaller compared to that of the 12-layer CORC® wire. In addition, the void space within each layer for these two types of cable was calculated and it was found that the void space was about 81%–86%. The main reason of critical current degradation is thus the different winding angle of each layers and the layers interaction, while the tape gap between tapes in same layer is only exacerbates degradation.

4. Conclusion

Analytical and FE models that combine the mechanical response and T-A methods were established to evaluate the strain distribution, inter-layer interaction, and their effect on the critical current of CORC® wires under applied axial tensile strain.

The strain distribution of individual tapes in CORC® wires, with up to 14 layers of tape, the distribution of the normal contact force and tangential friction between tapes and core under axial applied tensile strain were investigated for different cabling parameters, such as winding angle, core radius and core material. The results show that the winding angle and Poisson's ratio of the core are key factors affecting the CORC® wire performance under axial applied tensile strain. A smaller winding angle (25°–30°) and higher Poisson's ratio of the core can greatly improve the tensile performance of the CORC® wire. It is also found that if the winding angle of adjacent tape layers changes considerably, the radial contraction of the two layers also differs significantly. As a result, local excessive strain concentrations are created at the locations of the gaps between the tapes in each layer by inter-layer compression.

The analysis shows that for multi-layer CORC® wires, the change in winding angles of subsequent layers should be minimized. The cable's irreversible tensile strain limit can be significantly increased to 7%, when the tape helical winding angle is set around 30°. It is expected that these conclusions can be used to design CORC® wires with optimal performance.

Data availability statement

All data that support the findings of this study are included within the article (and any supplementary files).

Acknowledgments

This work was supported by the National Natural Science Foundation of China (12072136); and the China Scholarship Council (awarded to Keyang Wang for 2 year's study abroad at the University of Twente), and the U.S. Department of Energy, Offices of High Energy Physics and Fusion Energy Sciences under Grant Nos. DE-SC0014009, DE-SC0018125 and DE-SC0020710.

ORCID iDs

K Wang https://orcid.org/0000-0001-5858-5396
Y W Gao https://orcid.org/0000-0002-9536-0070
D C van der Laan https://orcid.org/0000-0001-5889-3751
A Nijhuis https://orcid.org/0000-0002-1600-9451

References

[1] Zanino R, Ciazynski D, Mitchell N and Richard L S 2005 Coupled mechanical–electromagnetic–thermal–hydraulic effects in Nb_3Sn cable-in-conduit conductors for ITER *Supercond. Sci. Technol.* **18** S376–S382
[2] Qin J, Wu Y, Warnet L L and Nijhuis A 2011 A novel numerical mechanical model for the stress–strain distribution in superconducting cable-in-conduit conductors *Supercond. Sci. Technol.* **24** 065012
[3] Ekin J W 1977 Mechanisms for critical-current degradation in NbTi and Nb_3Sn multifilamentary wires *IEEE Trans. Mag.* **13** 127–30
[4] Li L, Cheng J, Ni Z, Wang H, Dai Y and Wang Q 2015 Preliminary mechanical analysis of a 9.4-T whole-body MRI magnet *IEEE Trans. Appl. Supercond.* **25** 4400207
[5] Goldacker W, Grilli F, Pardo E, Kario A, Schlachter S I and Vojenciak M 2014 Roebel cables from REBCO coated conductors: a one-century-old concept for the superconductivity of the future *Supercond. Sci. Technol.* **27** 093001
[6] Zhai Y, Titus P, Kessel C and EI-Guebaly L 2018 Conceptual magnet design study for fusion nuclear science facility *Fusion Eng. Des.* **135** 324–36
[7] Barth C 2013 *High Temperature Superconductor Cable Concepts for Fusion Magnets* (Germany: KIT Scientific Publishing)
[8] van der Laan D C, Noyes P D, Miller G E, Weijers H W and Willering G P 2013 Characterization of a high-temperature superconducting conductor on round core cables in magnetic fields up to 20 T *Supercond. Sci. Technol.* **26** 045005
[9] van der Laan D C and Ekin J W 2007 Large intrinsic effect of axial strain on the critical current of high-temperature superconductors for electric power applications *Appl. Phys. Lett.* **90** 052506
[10] Llin K *et al* 2015 Experiments and FE modeling of stress-strain state in ReBCO tape under tensile, torsional and transverse load *Supercond. Sci. Technol.* **28** 055006
[11] Cheggour N, Stauffer T, Starch W, Lee P, Splett J, Goodrich L and Ghosh A 2018 Precipitous change of the irreversible strain limit with heat treatment temperature in Nb_3Sn wires made by the restacked-rod process *Sci. Rep.* **8** 13048
[12] Goldacker W, Frank A, Kudymow A, Heller R, Kling A, Terzieva S and Schmidt C 2009 Improvement of superconducting properties in ROEBEL assembled coated conductors (RACC) *IEEE Trans. Appl. Supercond.* **19** 3098–101
[13] Kario A, Vojenciak M, Grilli F, Kling A, Ringsdorf B, Walschburger U, Schlachter S I and Goldacker W 2013 Investigation of a Rutherford cable using coated conductor Roebel cables as strands *Supercond. Sci. Technol.* **26** 085019
[14] Celentano G, De Marzi G, Fabbri F, Muzzi L, Tomassetti G, Anemona A, Chiarelli S, Seri M, Bragagni A and Della Corte A 2014 Design of an industrially feasible twisted-stack HTS cable-in-conduit conductor for fusion application *IEEE Trans. Appl. Supercond.* **24** 4601805
[15] Ta W and Gao Y 2018 Numerical simulation of the electro-thermo-mechanical behaviors of a high temperature superconducting cable *Compos. Struct.* **192** 616–25
[16] Takayasu M, Chiesa L, Bromberg L and Minervini J V 2012 HTS twisted stacked-tape cable conductor *Supercond. Sci. Technol.* **25** 014011
[17] Takayasu M, Mangiarotti F J, Chiesa L, Bromberg L and Minervin J V 2013 Conductor characterization of YBCO twisted stacked-tape cables *IEEE Trans. Appl. Supercond.* **23** 4800104
[18] Takayasu M and Chiesa L 2015 Analytical investigation in bending characteristic of twisted stacked-tape cable conductor *Mater. Sci. Eng.* **102** 012023
[19] Hong W, Liu H, Liu F, Jin H and Yi S 2022 Improved calculation of magnetic hysteresis loss of stacked superconducting cable under T-A formulation *IEEE Trans. Appl. Supercond.* **32** 5900905
[20] van der Laan D C 2009 $YBa_2Cu_3O_{7-\delta}$ coated conductor cabling for low ac-loss and high-field magnet applications *Supercond. Sci. Technol.* **22** 065013
[21] Anvar V A *et al* 2018 Bending of CORC® cables and wires: finite element parametric study and experimental validation *Supercond. Sci. Technol.* **31** 115006
[22] Wang K, Gao Y, Luo W, Zhou Y and Nijhuis A 2021 Nonlinear contact behavior of HTS tapes during pancake coiling and CORC cabling *Supercond. Sci. Technol.* **34** 075003
[23] van der Laan D C, McRae D and Weiss J D 2019 Effect of monotonic and cyclic axial tensile stress on the performance of superconducting CORC® wires *Supercond. Sci. Technol.* **32** 054004
[24] van der Laan D C, Radcliff K, Anvar V A, Wang K, Nijhuis A and Weiss J D 2021 High-temperature superconducting CORC® wires with record-breaking axial tensile strain tolerance present a breakthrough for high-field magnets *Supercond. Sci. Technol.* **34** 10LT01
[25] Anvar V A, Wang K, Weiss J D, Radcliff K, van der Laan D C, Hossain M S A and Nijhuis A 2022 Enhanced critical axial tensile strain limit of CORC® wires: FEM and analytical modeling *Supercond. Sci. Technol.* **35** 055002
[26] Wang Y, Zhang M, Grilli F, Zhu Z and Yuan W 2019 Study of the magnetization loss of CORC® cables using

a 3D T-A formulation *Supercond. Sci. Technol.* **32** 025003

[27] Yang J, Li C, Tian M, Liu S, Shen B, Hao L, Ozturk Y and Coombs T 2022 Analysis of AC transport loss in conductor on round core cables *J. Supercond. Nov. Mag.* **35** 57–63

[28] Lai L and Gu C 2022 J model for studying AC magnetization loss in 3D cable structures *Supercond. Sci. Technol.* **35** 045008

[29] Phifer V, Small M, Bradford G, Weiss J, van der Laan D and Cooley L 2022 Investigations in the tape-to-tape contact resistance and contact composition in superconducting CORC® wires *Supercond. Sci. Technol.* **35** 065003

[30] Knapp R H 1979 Derivation of a new stiffness matrix for helically armored cables considering tension and torsion *Int. J. Numer. Meth. Eng.* **14** 515–29